2

A local uPAR-plasmin-TGFβ1 positive feedback loop in a computational model of angiogenic sprouting explains the *in vitro* effect of fibrinogen variants

This chapter is based on:

Sonja E. M. Boas, Marloes van den Broek, Ester M. Weijers, Pieter Koolwijk and Roeland M.H. Merks, *A local uPAR-plasmin-TGFβ1 positive feedback loop in a computational model of angiogenic sprouting explains the in vitro effect of fibrinogen variants* (in preparation)

background graphic: Photograph of the blood vessels in Sonja Boas' retina.

Abstract

We developed a computational model of angiogenesis-like invasion of endothelial cells into fibrin matrices. Using an experimental assay of sprouting in three-dimensional fibrin matrices, which is the temporal scaffold formed during wound healing, was found that the composition of fibrin impacts the level of angiogenesis. There was more ingrowth on high molecular weight (HMW) than on low molecular weight (LMW) fibrin. It is unclear which mechanisms regulate where and how many ingrowth spots are formed in the endothelial cell monolayer. To address this question, we studied which mechanisms underlie the reduced angiogenic ingrowth on LMW compared to HMW with a hybrid, cell-based and continuum computational model that represents the experimental setup. Based on the model results, we propose that a local positive feedback mechanism between uPAR, plasmin and TGFβ1 selects cells in the monolayer for matrix invasion and subsequently consolidates sprouting. Plasmin-mediated fibrin degradation by an invading cell releases transforming growth factor β1 (TGFβ1) from the matrix and TGFβ1 subsequently stimulates locally the ability of that cell to increase fibrin degradation. This model predicts a reduced angiogenic ingrowth on LMW compared to HMW, when we included the experimental observation that LMW binds less TGFβ1 than HMW.

2.1 Introduction

Angiogenesis is the formation of new blood vessels to perfuse hypoxic regions, such as wounds, growing tumors, or tissue-engineered constructs, by the branching or splitting of existing vessels [1, 2, 12, 15]. During angiogenesis, a fibrin matrix is formed as a provisional scaffold by leakage of fibrinogen into the tissue [77]. To (re)establish the blood supply, endothelial cells (ECs) from nearby blood vessels invade this fibrin matrix [77]. Tissue engineering and medical therapies aim to control the level of angiogenesis and could benefit from a mechanistic understanding of angiogenesis in fibrin matrices [6, 12]. It is unclear which mechanisms regulate the onset of capillary formation or 'ingrowth spots' in an endothelial cell monolayer and consolidate further angiogenic sprouting.

The level of ingrowth spots and angiogenesis is strongly affected by the fibrin composition [39, 76, 78, 79]. Weijers *et al.* [39] used an *in vitro* model of capillary-like tube formation in a three-dimensional fibrin matrix, previously introduced by Koolwijk *et al.* [38], to study the effect of the fibrin composition on angiogenesis. A monolayer of human microvascular endothelial cells (HMVECs) is seeded on a fibrin matrix and sprouts grow into the fibrin matrix upon stimulation with an angiogenic factor, vascular endothelial growth factor (VEGF) and/or basic fibroblast growth factor (bFGF), in combination with

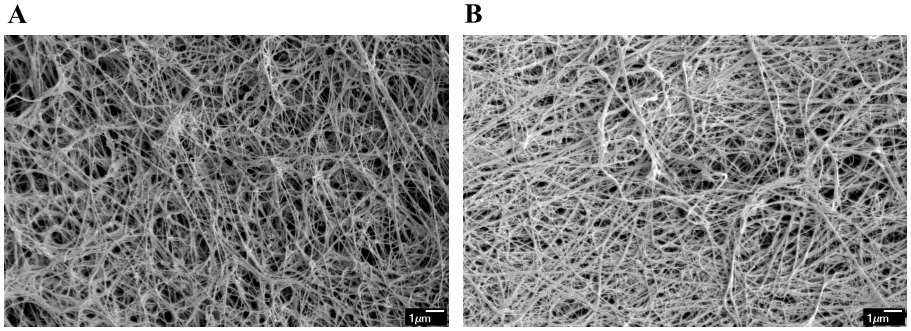

Figure 2.1: Fibrin matrices. Scanning electron microscopic analysis of (A) high molecular weight (HMW) fibrinogen and (B) low molecular weight (LMW) fibrinogen. HMW has thicker fibers and forms more open network structures than LMW. Bars represent 1 μm. The figures are derived from Kaijzel *et al.* [78].

the inflammatory mediator TNFα (tumor necrosis factor α). From now on we will refer to this *in vitro* model as the 'HMVEC-fibrin assay'. Fibrinogen naturally occurs in three different variants: HMW (high molecular weight) fibrinogen (Figure 2.1A), LMW (low molecular weight) fibrinogen (Figure 2.1B) and LMW' fibrinogen [39]. HMVECs proliferate more and show more angiogenic ingrowth on HMW fibrin than on LMW or unfractionated fibrin mixture [39]. In addition, the spacing between ingrowth spots is more wide-spread [80] than what would be expected from selection of tip cells through lateral inhibition by Dll4-Notch signaling [23, 24, 44, 45]. To study which mechanisms regulate the spacing of ingrowth spots and consolidate sprouting, we developed a computational model to evaluate a hypothetical mechanism for sprouting that could also explain a reduced ingrowth on LMW compared to HMW. This mechanism provides an alternative next to Dll4-Notch in leader cell or 'tip cell' selection [3, 21–23].

HMW and LMW differ in protein structure and after clotting result in different fibrin matrix structures. Polymerization of intact HMW fibrinogen results in HMW fibrin, whereas LMW fibrinogen, that lacks the C-terminus of one of the two Aα-chains of fibrinogen, forms LMW fibrin [39]. HMW fibrin has a more open matrix structure, with thicker fibers and larger openings between the fibers compared to LMW fibrin (see Figure 2.1). A simple explanation for the increased ingrowth on HMW fibrin compared to LMW fibrin could be that the ECs can invade the open matrix structure of HMW fibrin more easily. Furthermore, the mechanical properties could differ, which was shown to affect two-dimensional sprouting and network formation [69, 73, 74]. Additionally, HMVEC-associated fibrin degradation (fibrinolysis) is higher on HMW compared to LMW fibrin [39]. Finally, LMW fibrin has a reduced number of binding

sites for growth factors, e.g. TGFβ1 [81], that are located at the C-terminus of the Aα-chains. In this chapter we will focus on cell-associated fibrinolysis and protein binding.

Cell-associated fibrinolysis is mostly performed by the trypsin-like protease plasmin [19, 82–84]. Plasmin is the active conversion product of plasminogen, which is mainly produced by the liver and reaches fibrin scaffolds through the blood stream. Conversion of plasminogen into plasmin occurs by plasminogen activators and is highly regulated. Urokinase plasminogen activator (uPA) and tissue-type plasminogen activator (tPA) are secreted by ECs as single-chain proteins. tPA is expressed in quiescent endothelium [85] and is primarily involved in clot dissolution [86], whereas uPA and its cellular receptor (uPAR) are expressed during angiogenesis and control pericellular proteolysis [85, 87]. ECs secrete inactive, single chain pro-uPA. Pro-uPA binds to uPA receptors (uPARs) on the membrane of endothelial cells, and is subsequently converted into an active two-chained form. This active membrane-bound uPA-uPAR complex converts plasminogen into plasmin [19]. To balance fibrin degradation, ECs secrete plasminogen inhibitor type 1 (PAI-1) that binds to tPA and uPA for deactivation and the PAI-1-uPA-uPAR complex is internalized [82, 83]. Besides plasmin, membrane-type 1 metalloproteinase (MT1-MMP) can perform cell-associated fibrinolysis [88], but the MT1-MMP inhibitor TIMP-1 had only minor effects on angiogenesis in an assay similar to the HMVEC-fibrin assay, using a fibrin-10% collagen matrix [89]. In summary, the HMVEC-associated fibrinolysis [39] is due to the plasminogen-plasmin degradation system.

TGFβ1 has a strong pro-angiogenic effect in HMVEC cultured on Matrigel [90]. This pro-angiogenic effect depends on the upregulation of PAI-1 and uPAR by TGFβ1 and was inhibited by TGFβ1 antagonist peptides. TGFβ1 also induces PAI-1 and uPAR expression in hepatic stellate cells [91] and uPA/PAI-1 levels in human tumor tissues [92]. LMW has a reduced number of C-termini of the Aα-chain of fibrinogen compared to HMW. LTBP1 (latent transforming growth factor β (TGFβ) binding protein 1) potentially binds the C-terminus of this Aα-chain: the level of LTBP1 is dramatically reduced in LMW fibrinogen fraction I-9, which lacks major parts of the C-termini of the Aα-chain, compared to commercially available fibrinogen and intact fibrinogen fraction I-2 [81]. LTBP1 sequesters latent-TGFβ1 in the plasma to fibrin, resulting in an inactive TGFβ1 reservoir that can locally be activated and released by plasmin [20, 93]. In summary, the reduced number of LTBP1 binding sites in LMW compared to HMW can result in a lower bio-availability of TGFβ1, which could affect angiogenesis.

Based on the experimental data of cell-associated fibrinolysis and TGFβ1, we suggest that a local uPAR-plasmin-TGFβ1 positive feedback loop drives angiogenesis (see Figure 2.2): cell-bound uPAR activates plasmin (Figure 2.2,

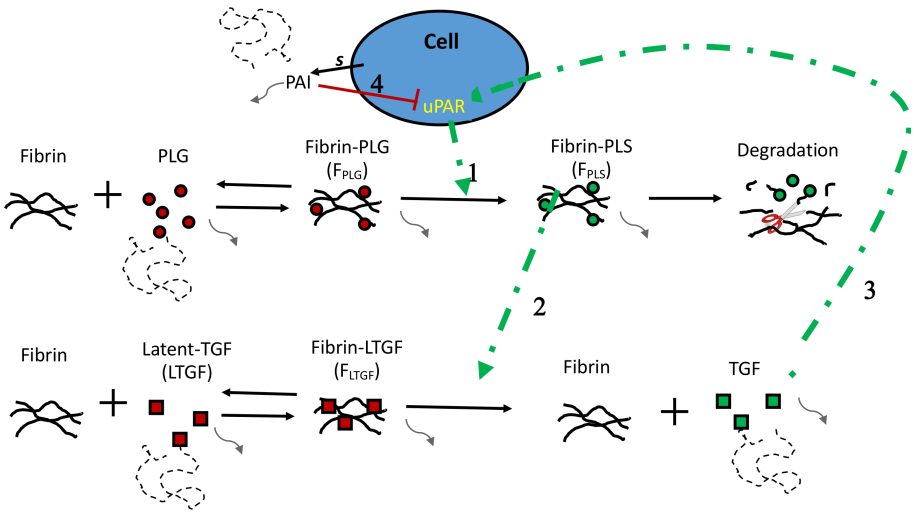

Figure 2.2: Schematic overview of plasmin and TGFβ1 interactions. Plasminogen (PLG) reversibly binds fibrin, forming fibrin-bound plasminogen (F_{PLG}). F_{PLG} is converted by cell-bound uPAR (arrow 1) to fibrin-bound plasmin (F_{PLs}). F_{PLS} degrades fibrin. Latent-TGFβ1 ($LTGF$) binds fibrin reversibly. Fibrin-bound latent-TGFβ1 (F_{LTGF}) is activated and released by F_{PLS} (arrow 2), resulting in active, diffusive TGFβ1 and free fibrin. Active TGFβ1 induces production of uPAR (arrow 4). Cells secrete (s) PAI-1 (PAI), which inhibits uPAR activity (arrow 4). The gray, dotted lines indicate diffusion of proteins and curved, gray lines indicate decay.

arrow 1), plasmin locally degrades fibrin and releases active TGFβ1 (see Figure 2.2, arrow 2), and TGFβ1 upregulates uPAR production in the protruding cell (see Figure 2.2, arrow 3), whereas nearby cells which experience only mild TGFβ1-dependent uPAR stimulation are silenced by self-secreted PAI-1 (see Figure 2.2, arrow 4).

In this hypothesis, cells are activated to degrade the matrix by an external growth factor. This mechanism for capillary sprout formation was first introduced in a mathematical model of Levine *et al.* [94]. This continuum model, which models cells and matrix as densities, shows that cells in a capillary aggregate into a bimodal structure to sprout towards a nearby tumor. The tumor secretes a growth factor and the location of capillary onset depends on the shape of the growth factor gradient. In the HMVEC-fibrin assay, it is unpredictable which cells in the monolayer become sprout leaders. To study what causes such a spontaneous onset of ingrowth, we do not include a growth factor gradient as was done by Levine *et al.* [94] and others [16, 51, 52, 65]. Nor do we bias the location of capillary onset by initializing with a leading cell in the monolayer as we did in a previous model [75] that represented the HMVEC-fibrin assay.

To study our hypothesis that an uPAR-plasmin-TGFβ1 positive feedback loop could account for spontaneous ingrowth, we model the plasminogen-plasmin degradation system in detail. This system is extensively studied in cell-free models [43, 95, 96]. We based the plasminogen-plasmin system in our model on the cell-free system of Diamond & Anand [95], which was used to predict lysis-fronts across fibrin clots for different administration regimes for tPA and uPA. The continuum model by Chaplain & Lolas [48] studied how the spatiotemporal dynamics of the plasmin system affect tumor invasion, using a fairly detailed description of the plasminogen-plasmin system: endothelial cells secrete uPA and PAI-1, plasmin is activated in proximity of uPA and cells, and PAI-1 scavenge uPA and plasmin. Our question requires a cell-based approach, rather than a continuum approach, because the physical interactions between cells and fibrin are important for locally triggering the positive feedback loop. Previous cell-based models of matrix invasion showed how an interplay of cell behaviors, such as haptotaxis towards higher concentrations of matrix proteins or chemotaxis towards higher concentrations of growth factor, drive sprouting and branching [51, 52, 65, 75]. These models did not focus on the details of matrix degradation, but simplified it to the secretion of proteolytic enzymes to degrade the extracellular matrix. We constructed a hybrid, cell-based and continuum computational model that combines a detailed description of cell-fibrin interactions, the plasminogen-plasmin system and the activation of proteolytic cellular activity by the growth factor TGFβ1.

2.2 Results

To study by what mechanism the level of angiogenesis is reduced on LMW compare to HMW fibrin, we developed a computational model that mimics the HMVEC-fibrin assay. The hybrid, cell-based and continuum computational model represents a cross-section of the *in vitro* model (Figure 2.3). The model is initialized with a monolayer of fifty endothelial cells on top of a fibrin matrix. Fibrin forms a physical obstruction for cells, while at the same time, fibrin offers cells support as cells can adhere to fibrin. Using cell-based modeling, we explicitly model cell shape, cell motility, cell-cell adhesion, and cell-fibrin adhesion. Each cell has a concentration of active uPAR homogeneously spread over its membrane and each cell secretes PAI-1. PAI-1, fibrin, latent-TGFβ1, active TGFβ1, plasminogen and plasmin are modeled as concentration fields and interact with each other, resulting in a local activation of plasminogen by cell-bound uPAR into plasmin (Figure 2.2). This releases and activates latent-TGFβ1 and degrades fibrin. Active TGFβ1 induces the production of uPAR in nearby cells, resulting in a local positive feedback loop that drives fibrin degradation. Cells can invade regions where fibrin is degraded, driven by adhesion of cells to the fibrin and contact-inhibited cell division.

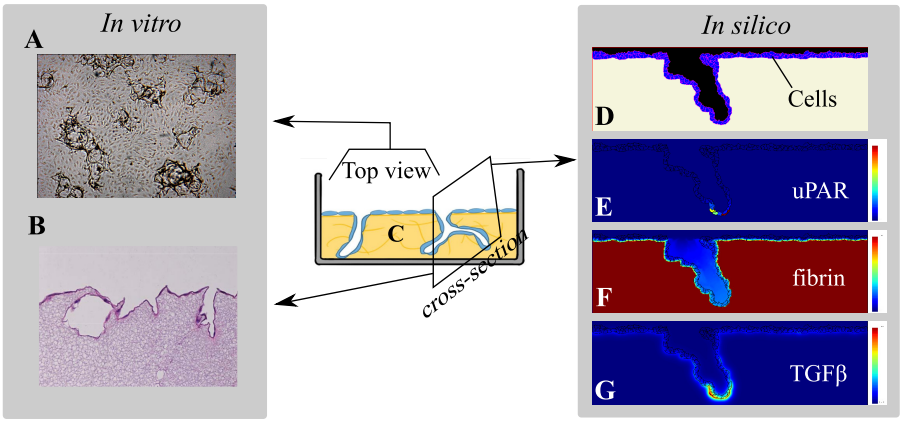

Figure 2.3: *In vitro* and *in silico* model setup. The HMVEC-fibrin assay can be studied with (A) nonphase contrast views of the monolayer or by (B) histological staining of cross-sections of the matrix after fixation. (C) A schematic illustration of the model is shown in the middle, with a monolayer of endothelial cells (blue) that form capillary-like tubes in a fibrin matrix (yellow). Images of an *in silico* simulation that represents a cross-section of the *in vitro* model are shown on the right. (D) Endothelial cells and fibrin are modeled with the CPM, (E) the uPAR concentration of cells is modeled with an ODE equation, and a PDE system calculates the concentration of (F) fibrin, (G) TGFβ1, PAI-1, PLG, PLS and all fibrin-bound forms (not shown).

To represent cells and their physical interactions with the fibrin matrix, the cellular Potts model [61, 62] was used. Cells are projected as patches of lattice sites on a lattice and move by copying lattice sites inward or outward, representing the extension and retraction of filopodia. A time step in the model, also called Monte Carlo step (MCS), represent approximately 2.5 minutes and a simulation takes 10 days similar to the HMVEC-fibrin assay [38].

The concentration of uPAR for each cell is modeled by one ordinary differential equation (ODE). A concentration field for uPAR is projected on the CPM grid, with each lattice site that is occupied by a cell having the uPAR concentration of that cell. The concentration of uPAR moves along with the location of the cell after cell movement. A system of coupled partial differential equations (PDEs, see Section 2.4.3) describes the reactions between fibrin, TGFβ1, plasminogen, plasmin, PAI-1 and all fibrin-bound forms. The plasminogen-plasmin system in this model is based on the cell-free model by Diamond & Anand [95] that studies the penetration of uPA and tPA in a fibrin clot present in the blood stream. To make it suitable for our question, we include the uPAR-plasmin-TGFβ1 positive feedback, simplified the implementation of fibrinolysis, and removed blood flow.

To model the plasminogen-plasmin degradation system and the uPAR-

plasmin-TGFβ1 positive feedback, we made the following assumptions:

1. Cell-bound uPAR carries out active proteolysis. We do not consider the activity of t-PA, because addition of tPA specific antibodies does not have a significant effect on the formation of capillary-like tubular structures in the HMVEC-fibrin assay.
2. Plasminogen binds fibrin reversibly.
3. Fibrin-bound plasminogen is converted to fibrin-bound plasmin by uPAR. Plasminogen is in a closed configuration in circulation, but binding to fibrin induces an open configuration that is much more susceptible for activation [97–99].
4. Plasmin remains fibrin-bound. As a result, plasmin is localized at the cell surface or in immediate proximity of the cell [100].
5. Endothelial cells secrete PAI-1, which diffuses and decays [19, 38]
6. PAI-1 inhibits uPAR activity by internalization of uPAR-PAI-1 complexes [82, 83]
7. Latent-TGFβ1 binds fibrin reversibly [20], we thereby implicitly model binding of LTBP1 to latent-TGFβ1.
8. We assume a non-competitive binding of latent-TGFβ1 and plasminogen for fibrin.
9. Fibrin-bound latent-TGFβ1 is activated and released by plasmin, resulting in diffusive TGFβ1 [20].
10. TGFβ1 induces expression of uPAR [90]
11. Plasminogen and latent-TGFβ1 are bound to fibrin at initialization. We assume that plasminogen and latent-TGFβ1 are readily bound to plasma-derived fibrin or are present in the serum and bind during the preparation of the fibrin matrix.

2.2.1 uPAR-plasmin-TGFβ1 positive feedback selects 'uPAR-rich' cells in the monolayer

In the HMVEC-fibrin assay, only a few cells in the monolayer end up with a high uPAR concentration [80] to lead invasion of sprouts. The selection mechanism of the 'uPAR-rich' cells in the monolayer is not completely understood. We used the model to test if the uPAR-plasmin-TGFβ1 positive feedback mechanism can select for uPAR-rich cells in the monolayer. For this purpose, we initialized each cell in the monolayer with the same level of uPAR (Figure 2.4A). Random cell movements change the contact-level and contact-duration with fibrin, resulting in local differences of plasmin activation. Fibrin is degraded at sites with a high plasmin activity (Figure 2.4B), and TGFβ1 is released from the matrix (Figure 2.4C). Released TGFβ1 induces the expression of uPAR in nearby cells (Figure 2.4D). The expression of uPAR in more distant cells can also be somewhat induced by the released TGFβ1, but uPAR activity is counterbalanced by self-secreted PAI-1. Due to stochasticity, only a few cells in

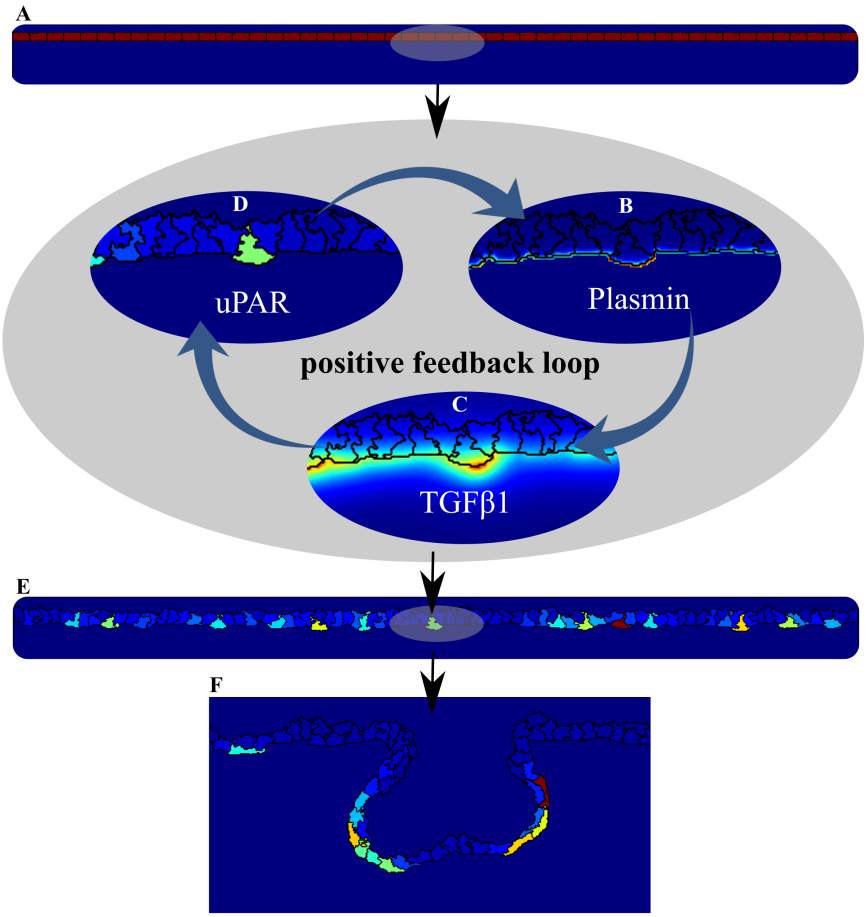

Figure 2.4: Spontaneous 'uPAR-rich' cell selection in the monolayer by a uPAR-plasmin-TGFβ1 positive feedback loop. (A) All cells in the model have the same uPAR concentration (the uPAR concentration in the cells is indicated by the red color) at initialization of a simulation. Local changes in fibrin-cell contact can increase (B) local plasmin concentration, resulting in degradation of fibrin and (C) release of active TGFβ1. (D) TGFβ1 can stimulate uPAR production. (E) The positive feedback loop selects 'uPAR-rich' cells in the monolayer, with a few cells having high level (red color) and most cells having low levels (blue color). (F) The positive feedback loop consolidates sprouting.

the monolayer are able to trigger the positive feedback loop sufficiently to overcome inhibition by PAI-1 and gain high levels of uPAR to start ingrowth (Figure 2.4E). In absence of fibrin-bound latent-TGFβ1, none of the cells in the monolayer, in a hundred stochastic simulations, manage to gain high levels of

uPAR due to the lack of TGFβ1-induced uPAR expression. Thus, our modeling results suggest that the uPAR-plasmin-TGFβ1 positive feedback loop might selects for uPAR-rich cells in a monolayer of endothelial cells to form ingrowth spots.

Once uPAR-rich cells are spontaneously selected in the monolayer, the uPAR-plasmin-TGFβ1 positive feedback consolidates sprout progression in the model (see Figure 2.4F and **Movie S1**). The cell that leads the sprout, which we will refer to as the tip cell, has the highest concentration of uPAR (see Figure 2.4F). This is in agreement with experimental observations [80]. As commonly observed *in vitro*, in the model sprouts can spontaneously branch (see Figure 2.4F and **Movie S1**). This occurs when a cell neighboring the tip cell also becomes a tip cell and moves into another direction, or when a cell higher up the sprout manages to trigger the feedback loop and starts a branch.

2.2.2 TNFα stimulates sprouting by inducting of uPAR activity

Sprouts are not formed in every simulation; sometimes due to stochasticity none of the cells are able to activate the positive feedback loop sufficiently to overcome the inhibition of PAI-1. Similarly, ingrowth is not seen in every experiment in the *in vitro* HMVEC-fibrin assay, but is highly variable per cell donor and even per assay with cells from the same donor. *In vitro*, TNFα is required to induce sprouting [38] and the mean tube length increases at higher doses of TNFα. TNFα increases uPA production and the level of cell-bound uPA [38]. Thus, addition of TNFα likely increases uPAR activity in all cells in the endothelial cell monolayer. We asked how it is possible that a global induction of uPAR activity by TNFα increases the number of local ingrowth spots, rather than causes excessive fibrinolysis and a subsequent lowering of the complete endothelial cell monolayer?

We used our model to test whether an increase of the production of uPAR in all cells would increase sprout frequency and the angiogenesis level. To mimic the effect of TNFα, we increased the constant production rate of uPAR. We found that the frequency of successful sprouting in a set of simulations increases with higher constant uPAR production rates (Figure 2.5). Figure 2.5A shows a set of simulation results after ten days of sprouting for a constant uPAR production rate of 0.001, 0.002, 0.003, and 0.005 (relative units (RU)/MCS). The quantitative level of the constant uPAR production level is experimentally not known, therefore we express the concentration relative to the concentration of the initial plasminogen concentration in the model. There is a more extensive ingrowth and a higher frequency of successful sprouting in simulations with higher constant uPAR production rates. Each set contains four stochastic simulation results for the same parameter settings and clearly shows the strong diversity in ingrowth frequency and sprout morphology.

To quantify sprouting, we used three measures: the angiogenesis level, the sprouting frequency and the fibrinolysis level. The angiogenesis level simultaneously reflects sprout depth and sprout count (see Section 2.4.2 for the quantification method). The blue curve in Figure 2.5B represents the mean angiogenesis level for all simulations that formed sprouts (angiogenesis level>0). The sprouting frequency is the number of simulations out of a hundred simulations that formed sprouts (red curve in Figure 2.5B). The fibrinolysis level, quantified as the mean percentage of initial fibrin lattice sites that are invaded by the endothelial cells in all hundred simulations, also increases for higher constant uPAR production rates, as is expressed by the green curve in Figure 2.5B.

In summary, an increase of the basal uPAR activity in all cells increases the chance that a cell in the monolayer can trigger the uPAR-plasmin-TGFβ1 positive feedback loop and gain high levels of uPAR for ingrowth. As a consequence, sprouts form more frequently and more excessively. The feedback loop functions locally, such that sprouts form rather than that the entire endothelial cell monolayer lowers by overall fibrinolysis. Thus, our model gives a mechanistic explanation of how the global stimulation of uPAR activity by TNFα might induce local sprouting.

2.2.3 Validation experiments

As a validation of the model, we tested whether it could reproduce the outcome of three published *in vitro* experiments of the plasminogen-plasmin degradation system.

Firstly, Koolwijk *et al.* [38] reported that there was no angiogenenic ingrowth and tubule formation in fibrin matrices that were made using plasminogen-depleted fibrinogen. In agreement, Figure 2.6A shows that there is no ingrowth in our model for low initial levels of fibrin-bound plasminogen. The sprouting percentage, the fibrinolysis percentage, and the angiogenesis level all increase when the initial fibrin-bound plasminogen concentration is increased. Plasminogen was expected to be rate limiting in plasmin-dependent fibrin degradation as plasmin is the conversion product of plamsinogen.

Secondly, inhibition of uPAR-bound uPA activity by addition of uPA specific polyclonal antibodies, or prevention of the binding of uPA to uPAR by soluble uPAR or blocking antibodies inhibited capillary-like tube formation dose-dependently [38, 80]. We modeled the inhibition of uPAR activity by an increase of the decay rate of uPAR. Consistent with the experimental results, Figure 2.6B shows that an increase in the decay rate of uPAR decreases the sprouting percentage, the fibrinolysis percentage, and angiogenesis level. Inhibition of uPAR activity was expected to reduce cell-associated fibrinolysis required for angiogenesis, since uPAR converts plasminogen into plasmin.

Thirdly, experiments show that there is an optimum PAI-1 concentration for

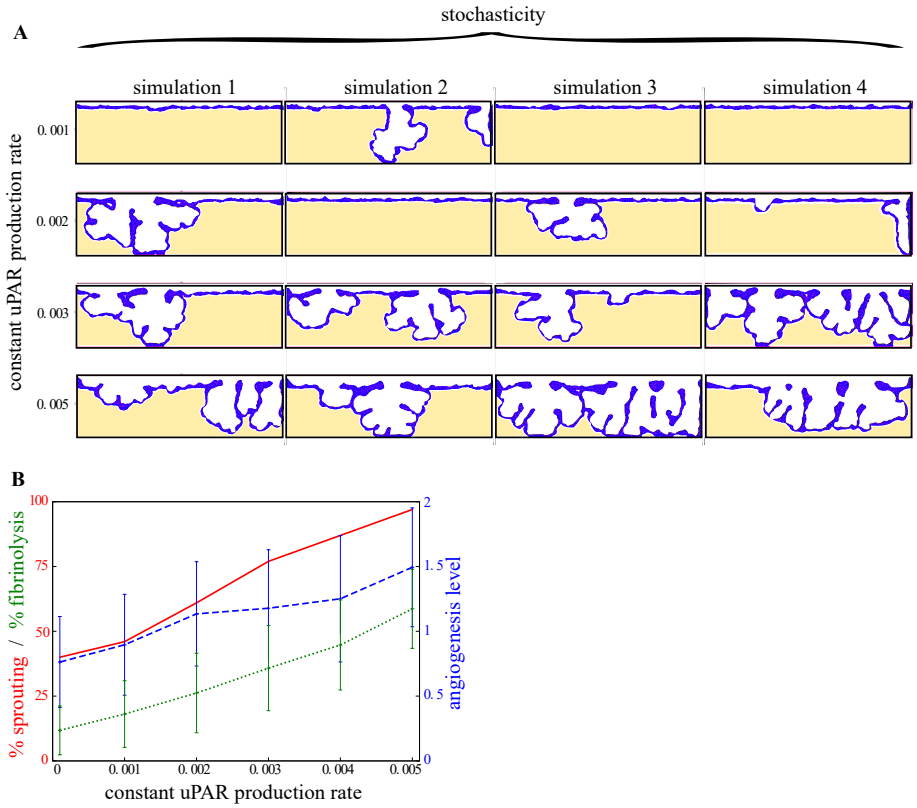

Figure 2.5: The angiogenesis level is sensitive to the constant uPAR production rate. Panel A shows a set of four stochastic simulation results at Monte Carlo step (MSC) 6000 for a constant uPAR production rate of 0.001, 0.002, 0.003, and 0.005 (relative units/MCS). Sprouts form more frequently and more extensively at higher constant uPAR production rates. For all simulations that formed sprouts, the mean angiogenesis level (blue curve) is calculated, representing the sprout count and sprout depth. The red curve in (B) represents the percentage of simulations that formed sprouts at MCS 6000 out of a hundred simulations. The green curve in (B) represents fibrinolysis, it is the mean (out of a hundred simulations) percentage of the initial fibrin lattice sites that are invaded by the endothelial cells at MCS 6000.

angiogenesis [101]: addition of PAI-1 to implants in wild-type mice enhanced angiogenesis up to 3-fold at low concentrations but inhibited angiogenesis nearly completely at high concentrations. Absence of protease inhibitors results in excessive fibrinolysis, which is incompatible with normal capillary formation [102, 103]. As for uPAR, we modeled the manipulation of PAI-1 activity by an increase of the decay rate of PAI-1. Figure 2.6C shows that the fibrinolysis percentage strongly increases when the decay rate of PAI-1 is increased.

High decay rate of PAI results in low PAI-1 activity, and thus in excessive fibrinolysis; no sprouts are formed, but the entire monolayer lowers simultaneously. Low decay rates of PAI-1 result in high PAI-1 activity and sprouting is completely inhibited. Only for intermediate levels of PAI-1 activity, we find sprouting, indicated by the peaks in Figure 2.6C for the sprouting percentage and the angiogenesis level.

In conclusion, the model can reproduce three essential validation experiments for the plasminogen-plasmin system. In absence of fibrin-bound latent-TGFβ1, no sprouts are formed in all hundred simulations with a parameter set for which sprouts formed well in presence of fibrin-bound latent-TGFβ1 in Figure 2.5B and 2.6 (constant uPAR production rate=0.005 RU/MCS, initial fibrin-bound plasminogen concentration=1 RU, PAI-1 decay rate=0.01 MCS^{-1}, and uPAR decay rate=0.0095 MCS^{-1}). This shows that initialization and consolidation of sprouting truly depends on the uPAR-plasmin-TGFβ1 positive feedback in our model.

2.2.4 The bio-availability of TGFβ1 regulates the level of angiogenesis in HMW and LMW

As a next step, we used our model to design new hypotheses about the mechanisms that reduce the level of angiogenic ingrowth on LMW compared to HMW. The level of LTBP1 is dramatically reduced in LMW fibrinogen fraction I-9, which lacks major parts of the C-termini of the Aα-chain, compared to commercially available fibrinogen and intact fibrinogen fraction I-2 [81]. As LTBP1 sequesters latent-TGFβ1 to fibrin, this could result in a lower level of fibrin-bound latent-TGFβ1. We hypothesize that this reduced level of fibrin-bound latent TGFβ1, in combination with our suggested local uPAR-plasmin-TGFβ1 positive feedback, could cause the reduced level of angiogenesis on LMW compared to HMW. If the levels of inactive TGFβ1 in the fibrin matrix are too low, cells are not able to induce a strong enough uPAR-plasmin-TGFβ1 positive feedback loop to overcome the inhibition of PAI-1 and thus will not form sprouts.

In line with this hypothesis, Figure 2.7A shows that the sprouting percentage, the fibrinolysis percentage, and the angiogenesis level decrease with lower initial concentrations of fibrin-bound latent TGFβ1 in our model. In conclusion, our simulations results suggest that the angiogenic ingrowth is reduced on LMW compared to HMW due to a reduction in binding sites for LTBP1.

The addition of active TGFβ1 has a biphasic effect on *in vitro* sprouting [40], quantified by measuring the total length of all cellular structures that have penetrated beneath the surface monolayer. Addition of active TGFβ1 to the assay stimulates sprouting at low doses and inhibits sprouting at high doses of TGFβ1 [40]. In previous work, Pepper *et al.* [104] showed that TGFβ1 reduces bFGF-induced extracellular proteolysis and this could explain the re-

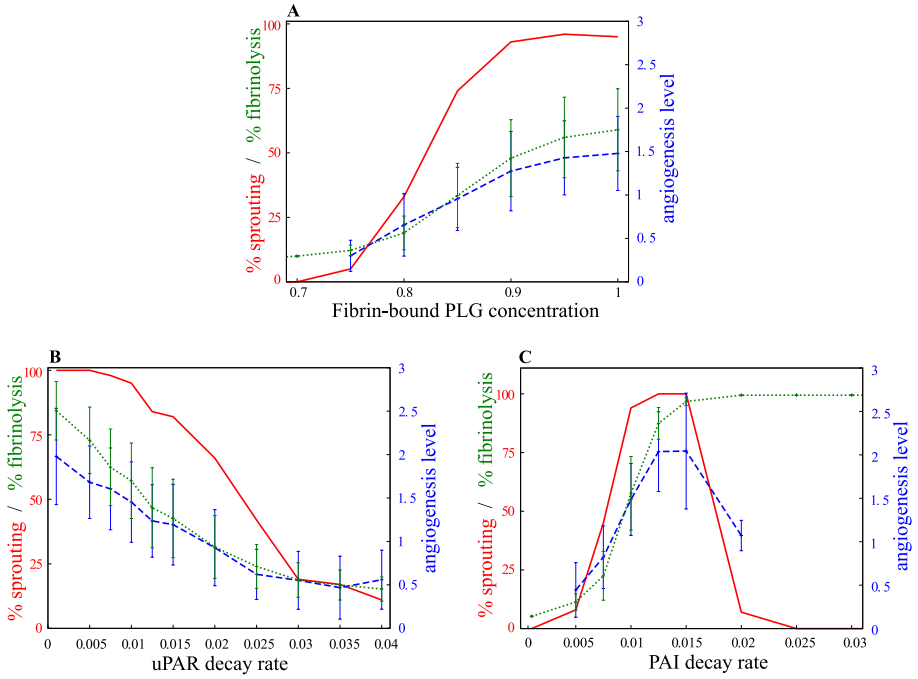

Figure 2.6: Model validation experiments. The sprouting percentage (red curve), the angiogenesis level (blue curve), and the fibrinolysis percentage (green curve), are plotted against changes in (A) the initial concentration of fibrin-bound plasminogen (relative units), (B) the decay rate of uPAR (MCS^{-1}), and (C) the decay rate of PAI-1 (MCS^{-1}). The sprouting percentage is the percentage of simulations (out of a 100 simulations) that have an angiogenesis level larger than zero. The angiogenesis level is a measure that simultaneously reflects sprout depth and sprout count, and the mean angiogenesis level is taken over all simulations that actually formed sprouts. The fibrinolysis percentage is the percentage of the initial fibrin lattice sites that are invaded by the endothelial cells at MCS 6000.

duced invasion at high doses of TGFβ1 [40]. To test this biphasic effect in the model, we initialized the model with a homogeneously spread concentration of active TGFβ1. The medium containing TGFβ1 is refreshed every two days *in vitro*, similarly we reset the TGFβ1 concentration to the initial value after every two days in the model. Figure 2.7B shows that TGFβ1 also has a biphasic effect on angiogenesis in the model. At low concentrations of added TGFβ1 (TGFβ1=0.5 and TGFβ1=10 in Figure 2.7B), more sprouts are formed than without addition of TGFβ1 (TGFβ1=0 in Figure 2.7B). The uPAR activity in all cells increases due to the overall addition of TGFβ1, allowing some cells to get over the inhibitory PAI-1 threshold for triggering the uPAR-plasmin-TGFβ1 positive feedback loop. This is a similar effect as was seen

for the stimulation with TNFα in Section 2.2.2. However, the upregulation of uPAR activity is too strong at high doses of TGFβ1, and consequently all cells degrade the matrix. This results in lowering of the complete endothelial cell monolayer, rather than in local sprouting (TGFβ1=1000 in Figure 2.7B) and sprouting is thus reduced. In this case, fibrin is quickly degraded and some cells loose contact with fibrin. Because the model only includes fibrin adhesion and contact-inhibited mitosis, these cells are no longer stimulated to migrate along with the degrading matrix and sometimes form a stack of cells above the monolayer. This is a model artefact, and these stacks of cells are not considered to be sprouts, but are considered to be part of the endothelial cell monolayer.

In conclusion, our model can reproduce the biphasic effect of TGFβ1 on angiogenesis, but the cause of the reduction of sprouting at high doses of TGFβ1 in our model is inconsistent with the proposed mechanism hereof by Pepper *et al.* [40]. Our model suggests that low doses of TGFβ1 increase the probability that cells in the monolayer can trigger the uPAR-plasmin-TGFβ1 positive feedback loop and start sprouting, whereas high doses of TGFβ1 reduce sprouting due to excessive matrix degradation. Unfortunately, the level of matrix degradation was not measured in the *in vitro* experiment by Pepper *et al.* [40]. Our current model does not include a negative feedback of TGFβ1 on bFGF-induced extracellular proteolysis. Future work should verify if a biphasic effect of TGFβ1 on angiogenesis, without excessive matrix degradation at high levels of TGFβ1, can be found in presence of such a feedback in our model.

2.3 Discussion

We developed a computational model to study what mechanisms cause angiogenic ingrowth and subsequent sprouting in a HMVEC-fibrin assay, in which endothelial cells form angiogenic-like tubule structures in fibrin matrices [38, 39]. For this purpose, we asked what mechanisms cause a reduced level of angiogenesis on LMW compared to HMW matrices [39]. Based on experimental data, we propose that an uPAR-plasmin-TGFβ1 positive feedback loop drives angiogenic sprouting. Model simulations that include this feedback loop show a spontaneous selection of 'uPAR-rich' cells in a monolayer of cells. Subsequently, the feedback loop allows for the 'uPAR-rich' cells to continue matrix invasion and sprouting. The model can reproduce several basic experimental observations of the plasminogen-plasmin degradation system. The model predicts a reduced level of angiogenesis on LMW compared to HMW, when the uPAR-plasmin-TGFβ1 positive feedback loop cannot be activated sufficiently for sprouting in LMW. This could be due to an experimentally observed [81] reduced level of TGFβ1 bound to LMW, which lacks major parts of the C-termini

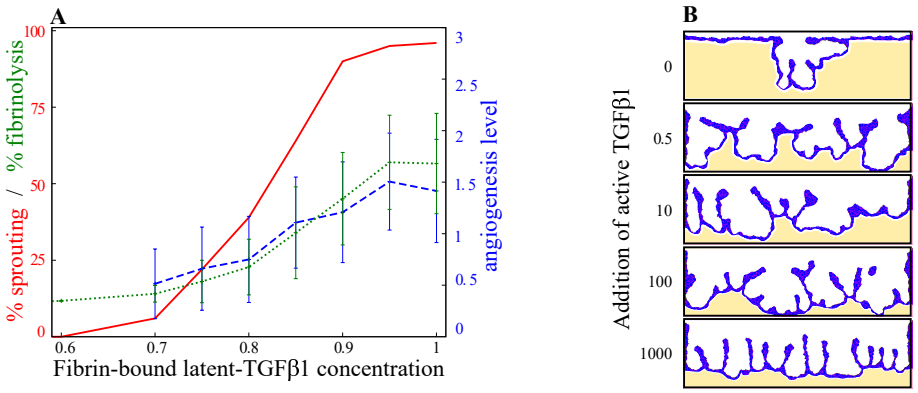

Figure 2.7: TGFβ1 experiments. (A) The sprouting percentage (red curve), the angiogenesis level (blue curve), and the fibrinolysis percentage (green curve), are plotted against changes in the initial concentration of fibrin-bound latent-TGFβ1 (relative units). The sprouting percentage is the percentage of simulations (out of a 100 simulations) that have an angiogenesis level larger than zero. The angiogenesis level is a measure that simultaneously reflects sprout depth and sprout count, and the mean angiogenesis level is taken over all simulations that actually formed sprouts. The fibrinolysis percentage is the percentage of the initial fibrin lattice sites that are invaded by the endothelial cells at MCS 6000. (B) Addition of active TGFβ1 has a biphasic effect on sprout formation in our model. The sprouting frequency increases for the addition of low doses of TGFβ1, but global degradation of the complete endothelial cell mololayer prevents sprout formation at high doses of TGFβ1.

of the Aα-chain, compared to HMW. In conclusion, the model gives a new mechanistic hypothesis for the driving mechanisms of angiogenic sprouting in the *in vitro* model.

The uPAR-plasmin-TGFβ1 positive feedback loop in our model causes a spontaneous selection of 'uPAR-rich' cells in the monolayer. Due to random cell movements, the feedback loop is activated more strongly by some cells than by others, resulting in autonomous selection of sprout leader cells in the monolayer. Due to stochasticity, in some simulations there no cells are able to activate the feedback loop sufficiently to overcome PAI-1 inhibition. Similarly, in our hands there is a large variation in the success of sprouting in the HMVEC-fibrin assay. We found that the basic production level of uPAR strongly regulates the probability that 'uPAR-rich' cells are locally selected and sprouts are formed. A possible candidate for the induction of uPAR activity is TNFα [38]. Addition of TNFα is required in the *in vitro* experiment to induce angiogenesis. Thus, our simulations provide an explanation for how a slight upregulation of uPAR activity by TNFα could induce sprouting.

Endothelial cells in the HMVEC-fibrin assay secrete the main inhibitor of the

plasmin system PAI-1 [38], but it is unknown if all cells, only the quiescent cells in the monolayer or perhaps only the invading uPAR-rich cells secrete PAI-1. The classic work by Turing [105] and Gierer & Meinhardt [106] shows that periodic patterns form when an inhibitor and an activator are secreted by the same cell. This requires that the activator stimulates the production of the activator and the inhibitor, and that the inhibitor diffuses faster than the activator. The self-activation locally increases the activator's concentration and overcomes the inhibition, while neighboring areas are silenced by the diffusing inhibitor. Interestingly, our uPAR-plasmin-TGFβ1 positive feedback loop matches this system, as the positive feedback loop drives local activation of uPAR, and the inhibitor PAI-1 diffuses, whereas uPAR only moves small distances by cell movement. We currently assumed that all cells secrete PAI-1, but it is very well possible that the uPAR-rich cells secrete most PAI-1, because TGFβ1 induces production of uPAR as well as PAI-1 in MVEC cultured on Matrigel [90]. In conclusion, to determine whether activator-inhibitor dynamics play a role in pattern formation of ingrowth spots in the monolayer in the HMVEC-fibrin assay, the localization of PAI-1 secretion should be determined.

Besides the activator-inhibitor system, the closely related substrate-depletion model [106] is a well-studied mechanism for pattern formation. In our model, plasminogen is the substrate for plasmin production. Conversion of plasminogen at sites of matrix invasion results in depletion of plasminogen in surrounding regions by diffusion. In agreement, plasminogen is a limiting factor for angiogenesis in the HMVEC-fibrin assay [38]. Plasminogen depletion has low impact in the current model, because we initialize with a high, homogeneously spread concentration of immobile fibrin-bound plasminogen. However, plasminogen binds fibrin reversibly, thus this mechanism might influence the location of ingrowth spots for lower levels of fibrin-bound plasminogen. Interestingly, there is a delay of sprout initiation when the model initializes with unbound PLG. It takes some time to reach sufficiently high concentrations of fibrin-bound plasminogen, which is then converted to plasmin by uPAR for matrix degradation.

Another patterning mechanisms that is involved in angiogenesis is lateral inhibition by Delta-Notch signaling [3, 21–23]. Cells that have high levels of Delta ligands on their membrane differentiate into so called 'tip cells', which are the leaders of sprouts, and cells with low levels of Delta become 'stalk cells' [23]. Lateral inhibition occurs by interaction of Delta ligands with the Notch receptor of neighboring cells, resulting in the suppression of Delta production in those neighbors [3, 21–23]. Lateral inhibition creates a pepper-and-salt pattern of tip and stalk cells, with tip cells surrounded by a rosette of stalk cells in monolayers *in silico* [44, 45]. The patterning of bristles in Drosophila epithelium becomes more sparse by Dll4-Notch signaling induced by long, dynamic filopodia that reach over several cell diameters in distance

[107]. However, the resulting pattern of bristles is still more fine-mazed and more regular than the observed pattern of uPAR-rich leader cells in the monolayer of the HMVEC-fibrin assay [80]. Thus, Delta-Notch signaling alone cannot account for this more widespread and irregular pattern. Possibly the involvement of another local regulation, such as our proposed uPAR-plasmin-TGFβ1 positive feedback loop, interferes with tip cell selection to make it more wide-spread. Notably, gene expression levels of Dll4 and Notch4 were significantly higher in endothelial cells cultured on LMW matrices than on HMW matrices [39]. The Dll4 and Notch4 expression differences by themselves cannot explain the reduced ingrowth on LMW, as specific inhibition of DLL4-Notch was unable to induce recovery of tube formation in LMW. In conclusion, local activation and lateral inhibition mechanisms might be involved in selection of ingrowth spots in the monolayer.

Furthermore, interference of Dll4-Notch signaling in the local degradation feedback loop could affect sprout morphology. In simulations of our current model, cells neighboring the leading tip cell are also somewhat activated by the released TGFβ1 and contribute to sprouting. This results in fairly wide, sometimes cyst-like sprouts. This is in agreement with results on sprout morphology from our previous model [75], in which we initialize with one predefined tip cell in the monolayer to model sprouting in the HMVEC-fibrin assay. Here, cyst-like sprouts also form when stalk cells contribute to matrix degradation, whereas narrow sprouts form when solely the tip cell secretes proteolytic enzymes for matrix degradation. We propose that one of the functions of lateral inhibition by Delta-Notch signaling could be to repress proteolytic activity of the stalk cells adjacent to the tip cell, such that only the tip cell degrades the matrix and thinner sprouts form.

Our model reproduces angiogenic sprouting by very simple sprouting dynamics, namely cell-fibrin adhesion and cell-division. However, the addition of TNFα in the *in vitro* model strongly inhibits cell division [38]. Many alternative mechanisms of cell migration and angiogenic sprouting have been proposed and are also tested *in silico*, such as haptotaxis towards higher concentrations of binding epitopes in fibrin [65], different forms of chemotaxis towards higher concentrations of growth factor [16, 63–66, 71], mechanotaxis towards higher regions of strains in the matrix [69], and preferential attraction to elongated structures [108]. Our model could be extended with such sprouting and cell migration mechanisms to replace cell division.

A detailed description of the plasminogen-plasmin system is included in our model, but still some simplifications were made. For instance, we did not take into account interactions with matrix metalloproteinases (MMPs). Membrane-type 1 metalloproteinase (MT1-MMP) can perform cell-associated fibrinolysis [88], but only plays a minor role in angiogenesis in the HMVEC-fibrin assay as the inhibitor TIMP-1 had only minor effects [89]. Furthermore, we neglected

the low proteolytic activity of pro-uPA [19], and only modeled active uPAR. Interactions between pro-uPA and plasmin could give some interesting dynamics. Venkatraman *et al.* [43] considered a positive feedback loop in which the initial cleavage of plasminogen into plasmin is more efficient by uPA than pro-uPA, and the conversion of pro-uPA to uPA is driven by plasmin. By the use of a cell-free model, they predict that uPA-plasmin activation is bistable in the presence of this positive feedback loop in combination with substrate competition for plasmin.

Our model predicts that the reduced level of angiogenesis on LMW compared to HMW fibrin could at least in part be explained by a reduced level of fibrin-bound latent-TGFβ1 in LMW. To validate this hypothesis, we propose to check if there is indeed a reduced level of fibrin-bound latent-TGFβ1 in LMW matrices in the *in vitro* HMVEC-fibrin assay. As a second experiment, we propose to validate whether angiogenesis can be reduced on HMW by addition of TGFβ1-antagonists. These validation experiments can bring us closer to a true understanding of the mechanisms that selects leader or 'tip cells' in the monolayer and consolidate sprouting in the HMVEC-fibrin assay.

2.4 Methods

We developed a hybrid, cell-based and continuum computational model of angiogenic sprouting to represent the *in vitro* HMVEC-fibrin assay (Figure 2.3). The model includes a uPAR-plasmin-TGFβ1 positive feedback loop that drives sprouting and is used to explain the reduced ingrowth on LMW compared to HMW. Cells and their physical interaction with fibrin are modeled with the cellular Potts model (CPM). The CPM is coupled to concentration fields to model the uPAR-plasmin-TGFβ1 positive feedback loop. Each cell has a concentration of uPAR, homogeneously spread on its membrane, modeled by an ordinary differential equation (ODE). A system of partial differential equations (PDEs) described the interactions between fibrin, plasminogen, plasmin, PAI-1 and TGFβ1.

2.4.1 Cellular Potts model

The model is initialized with a monolayer of fifty endothelial cells on top of a fibrin matrix and some medium on top (see Figure 2.8). These are enclosed by a border and a small immobile 'cell patch' is present in the border at the level of the monolayer, to mimic a continuous monolayer of cells.

The shape and motility of endothelial cells are modeled with the cellular Potts model (CPM) [61, 62]. The model domain is a two-dimensional, regular lattice $\Lambda \subset \mathbb{Z}^2$, with $\vec{x} \in \Lambda$ the coordinates in the lattice. Cells are projected on the lattice as patches of connected lattice sites. All lattice sites that belong to a cell are marked with the same unique identifier ($\sigma(\vec{x})$). Each identifier

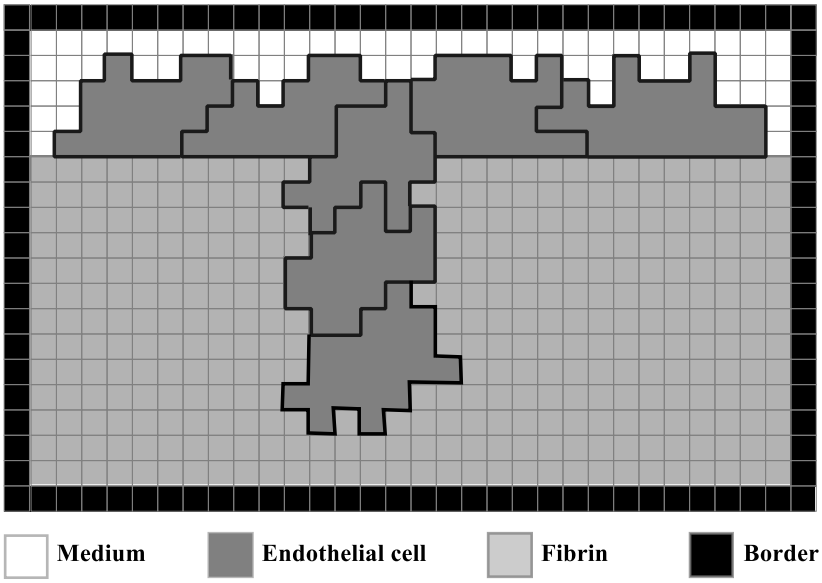

Figure 2.8: Schematic representation of the Cellular Potts model. The different colors depict the types defined in the computational model of the HMVEC-fibrin assay. A monolayer of endothelial cells is seeded on top of a fibrin matrix, with some medium on top. The modeling domain is surrounded with a border. Cells degrade fibrin, invade and form sprouts.

is associated with a type (τ), here $\tau = \{\text{cell, fibrin, cell patch, border, medium}\}$. Cells are motile, while fibrin, the border and the cell patch are static. Cells move by extending or retracting filopodia, modeled by copy attempts of the state (σ) of a randomly selected lattice site $\vec{x}$ into a randomly selected adjacent (second neighbor order) lattice site $\vec{x}\prime$ (see Figure 2.9). Whether such a copy attempt is excepted depends on the change of energy of the system (Hamiltonian) resulting from this copy. The Hamiltonian (H) of the system describes the forces resulting from cell behaviors and properties in the model. The cell behaviors and properties included in the model are cell adhesion, cell size, cell connectivity and fibrin invasion. A copy attempt is always accepted if it moves along a force and thus decreases the Hamiltonian. If a copy increases the Hamiltonian, the copy will be accepted according the Boltzmann probability function: $P_{\text{Boltzmann}}(H) = e^{\frac{-\Delta H}{\mu}}$, with μ representing active random membrane fluctuations. In one time step, a Monte Carlo step (MCS), as many copy attempts are performed as there are lattice sites in the lattice.

Cell adhesion. The energy resulting from adhesion is described as:

$$H_{\text{contact}} = \sum_{(\vec{x},\vec{x}\prime)} J(\tau(\sigma(\vec{x})), \tau(\sigma(\vec{x}\prime)))\,(1 - \delta(\sigma(\vec{x}), \sigma(\vec{x}\prime)))\,, \tag{2.1}$$

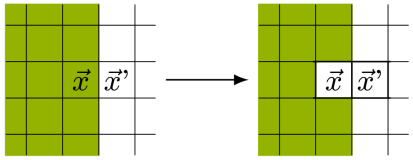

Figure 2.9: Graphical representation of a copy attempt. A random grid site ($\vec{x}$) is chosen to copy the state of a neighboring grid site ($\vec{x}\prime$) to simulate pseudopod extensions and retractions.

in which adhesion is restricted to the cell membrane by the Kronecker delta ($\delta(x,y) = 1, x = y, 0, x \neq y$) and $(\vec{x}, \vec{x}\prime)$ represents the set of all neighboring lattice site pairs. Each type combination has an adhesion energy $J_{\tau,\tau}$, with low values representing strong adhesion and high values weak adhesion or even repulsion.

Cell size. Cells have a preferred size (A) and deviation of their actual size (a) from this preferred size cost energy, following

$$H_{\text{size}} = \lambda_A(\sigma) \sum_{\sigma} \left(A(\sigma) - a(\sigma)\right)^2, \tag{2.2}$$

with λ_A representing cell elasticity.

Fibrin invasion. To model fibrin invasion, we coupled the CPM to a system of coupled PDEs that describes all kinetic reactions involved in the uPAR-plasmin-TGFβ1 feedback loop that we propose in this chapter. The PDE concentration fields are discretized on the CPM lattice. The probability that a cell invades fibrin, thus performs an extending copy into fibrin, depends on the total concentration of fibrin at the invaded fibrin pixel ($f(\vec{x}\prime)$). The total concentration of fibrin is the sum of all the PDE components that contain fibrin,

$$f(\vec{x}\prime) = F(\vec{x}\prime) + F_{\text{PLG}}(\vec{x}\prime) + F_{\text{PLS}}(\vec{x}\prime) + F_{\text{LTGF}}(\vec{x}\prime) + F_{\text{PLG,LTGF}}(\vec{x}\prime) + F_{\text{PLS,LTGF}}(\vec{x}\prime). \tag{2.3}$$

To model the physical obstruction of fibrin for cell invasion, a penalty of $H_{\text{invasion}} = \frac{1000}{1+e^{f(\vec{x}\prime)-0.5}}$ is added if $f(\vec{x}\prime) > 0.3$.

Mitosis. Every ten time steps, each cell has a probability (P_{mitosis}) to divide over its shortest axis if it is in little contact with other cell. More specifically, a cell may divide if $R_\sigma < R_{\text{mitosis}}$, with ($R_\sigma = \frac{\text{size membrane with cell-cell contact}}{\text{size total membrane}}$). The concentration of uPAR of the dividing cell is equally distributed over the daughter cells.

Model dimensions. The lattice size is $1000\mu m$ x $300\mu m$, with each lattice site representing $2\mu m$ x $2\mu m$. Sprouts fully develop in 6000 MCS in our model. Endothelial cells are cultured for 10 days in the HMVEC-fibrin assay [38], thus

a MCS is approximately 2.5 minutes. The parameter settings for the CPM are listed in Table 2.1. Accept for cell size (A), the parameters of the cellular Potts model can only be quantitatively coupled to experimental data.

Table 2.1: Parameters CPM.

$A = 800\ \mu m^2$	$\lambda_A = 100$	$\mu = 100$
$J_{\text{cell,Medium}} = 30$	$J_{\text{cell,cell}} = 15$	$J_{\text{fibrin,Medium}} = 120$
$J_{\text{cell,border}} = 1 \cdot 10^6$	$J_{\text{cell,fibrin}} = 75$	$H_{\text{connectivity}} = 1 \cdot 10^9$
$P_{\text{mitosis}} = 0.6$	$R_{\text{mitosis}} = 0.65$	$\Delta x = 2 \cdot 10^{-6}\ m$
lattice dimensions = 1000 μm x 300 μm		

2.4.2 Quantification of the angiogenesis level

The angiogenesis level simultaneously reflects sprout depth and sprout count. At the end of each simulation, the angiogenesis level is calculated as follows: 1) Ten equally distributed horizontal lines are drawn between 0 and 90 percent of initial fibrin matrix height. 2) For each line, the number of connected components consisting of cells or medium within fibrin are counted. Only the components larger than one cell size (20 lattice sites) and smaller than the complete line are counted. A component as large as the complete line would resemble lowering of the complete monolayer rather than sprouting. 3) The count of the ten lines is averaged.

2.4.3 Plasminogen-plasmin system and uPAR-plasmin-TGFβ1 positive feedback

The plasminogen-plasmin system in this model is based on the cell-free model by Diamond & Anand [95]. We made some changes to make it suitable for our question, most importantly we include the uPAR-plasmin-TGFβ1 positive feedback, simplified the implementation of fibrinolysis, and removed blood flow. Figure 2.10 shows an overview of the binding and conversion reactions of plasminogen and latent-TGFβ1 in relation to fibrin that are included in our model. In this section we will discuss the reactions in Figure 2.10 to explain the PDE system that describes the plasminogen-plasmin system and the uPAR-plasmin-TGFβ1 positive feedback loop.

2.4.4 Latent-TGFβ1 and plasminogen bind fibrin

Plasminogen (PLG) reversibly binds fibrin (F), forming fibrin-bound plasminogen (F_{PLG}). This reaction (reaction 1A in Figure 2.10) has a forward rate k_{f1} and a reverse rate k_{r1}. Similarly, the reversible binding of latent-TGFβ1 ($LTGF$)

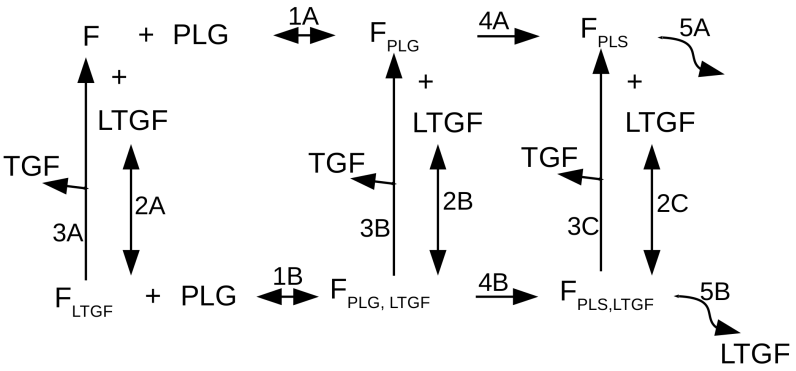

Figure 2.10: Overview of the binding and conversion reactions of plasminogen and latent-TGFβ1 in relation to fibrin. Plasminogen (*PLG*) and latent-TGFβ1 (*LTGF*) do not compete for binding with fibrin, thus fibrin can be unbound (F), bound solely by plasminogen (F_{PLG}), bound by solely latent-TGFβ1 (F_{LTGF}), or by both ($F_{\text{PLG,LTGF}}$). Plasminogen reversible binds fibrin (reactions 1A and 1B). Latent-TGFβ1 also reversible binds fibrin (reactions 2A, 2B, and 2C). Latent-TGFβ1 is released from fibrin by plasmin into the active form (*TGF*, reactions 3A, 3B, and 3C). Fibrin-bound plasminogen can be converted to fibrin-bound plasmin, either without (F_{PLs}, reaction 4A) or with ($F_{\text{PLS,LTGF}}$, reaction 4B) co-binding of latent-TGFβ1. Reactions 5A and 5B represent fibrinolysis, which can result in the release of latent-TGFβ1 (reaction 5B).

to fibrin (reaction 2A) depends on a forward rate k_{f2} and a reverse rate k_{r2}. *LTGF* that is bound to fibrin (F_{LTGF}) can be released and activated by plasmin-mediated proteolytic activity, resulting in active TGFβ1 and free fibrin (reaction 3A). This reaction follows Michaelis Menten kinetics with constants k_{u2} and k_{m2}. The change in concentration of fibrin depends on $PLG - Fibrin$ binding (1A), $LTGF - Fibrin$ binding (2A) and release of *TGF* (3A), following:

$$\frac{\partial F}{\partial t} = \overbrace{-PLG * F * k_{f1} + F_{\text{PLG}} * k_{r1}}^{PLG-Fibrin\ binding\ (1A)} + \overbrace{F_{\text{LTGF}} * k_{r2} - LTGF * F * k_{f2}}^{LTGF-Fibrin\ binding\ (2A)} + \overbrace{\frac{F_{\text{LTGF}} * (F_{\text{PLS}} + F_{\text{PLS,LTGF}}) * k_{u2}}{k_{m2} + F_{\text{LTGF}}}}^{Release\ TGF\ (3A)} \tag{2.4}$$

We assume that plasminogen and latent-TGFβ1 do not compete with each other for the binding sites in fibrin. Consequently, the rates of the reversible binding reaction of *PLG* to fibrin are equal to the rates for *PLG* binding to fibrin to which *LTGF* is bound (F_{LTGF}), thus reactions 1A and 1B in Figure

2.10 have the same rate constants. Plasminogen binding to F_{LTGF} forms $F_{\mathrm{PLG,TGFL}}$ (reaction 1B). *PLG* diffuses with diffusion coefficient D_{PLG} and decays with rate ϵ_{PLG}. The change in concentration of plasminogen depends on $PLG - Fibrin$ binding (1A), $PLG - F_{\mathrm{LTGF}}$ binding (1B), and its diffusion and decay, following:

$$\frac{\partial PLG}{\partial t} = \overbrace{D_{\mathrm{PLG}}\nabla^2 PLG}^{Diffusion} - \overbrace{\epsilon_{\mathrm{PLG}} PLG}^{Decay} + \overbrace{F_{\mathrm{PLG}} * k_{r1} - PLG * F * k_{f1}}^{PLG-Fibrin\ binding\ (1A)} + \overbrace{F_{\mathrm{PLG,LTGF}} * k_{r1} - PLG * F_{\mathrm{LTGF}} * k_{f1}}^{PLG-F_{\mathrm{LTGF}}\ binding\ (1B)} \quad (2.5)$$

Similarly, the reversible binding of *LTGF* to fibrin has equal rates for fibrin to which plasminogen or plasmin is bound, F_{PLG} and F_{PLS} respectively. Thus, reactions 2A, 2B and 2C in Figure 2.10 have the same rate constants. Unbound *LTGF* diffuses with diffusion coefficient D_{LTGF} and decays with rate ϵ_{LTGF}. *LTGF* is released from the matrix upon plasmin-mediated fibrinolysis (reaction 5B), modeled with a Hill equation with constant d. The change in concentration of latent-TGFβ1 depends on $LTGF - Fibrin$ binding (2A), $LTGF - F_{\mathrm{PLG}}$ binding (2B), $LTGF - F_{\mathrm{PLS}}$ binding (2C), release of *LTGF* (5B), and its diffusion and decay, following:

$$\frac{\partial LTGF}{\partial t} = \overbrace{D_{\mathrm{LTGF}}\nabla^2 LTGF}^{Diffusion} - \overbrace{\epsilon_{\mathrm{LTGF}} LTGF}^{Decay} + \overbrace{F_{\mathrm{LTGF}} * k_{r2} - LTGF * F * k_{f2}}^{LTGF-Fibrin\ binding\ (2A)} + \quad (2.6)$$

$$\overbrace{F_{\mathrm{PLG,LTGF}} * k_{r2} - LTGF * F_{\mathrm{PLG}} * k_{f2}}^{LTGF-F_{\mathrm{PLG}}\ binding\ (2B)} + \overbrace{\frac{F^2_{\mathrm{PLS,LTGF}}}{d + F^2_{\mathrm{PLS,LTGF}}}}^{Release\ LTGF\ (5B)} + \overbrace{F_{\mathrm{PLS,LTGF}} * k_{r2} - LTGF * F_{\mathrm{PLS}} * k_{f2}}^{LTGF-F_{\mathrm{PLS}}\ binding\ (2C)}$$

The change in concentration of fibrin-bound latent-TGFβ1 depends on $PLG - F_{\mathrm{LTGF}}$ binding (1B), $LTGF - Fibrin$ binding (2A), release of *TGF* (3A), and its decay, following:

$$\frac{\partial F_{\mathrm{LTGF}}}{\partial t} = -\overbrace{\epsilon_{F_{\mathrm{LTGF}}} F_{\mathrm{LTGF}}}^{Decay} + \overbrace{F_{\mathrm{PLG,LTGF}} * k_{r1} - PLG * F_{\mathrm{LTGF}} * k_{f1}}^{PLG-F_{\mathrm{LTGF}}\ binding\ (1B)} + \quad (2.7)$$

$$\overbrace{LTGF * F * k_{f2} - F_{\mathrm{LTGF}} * k_{r2}}^{LTGF-Fibrin\ binding\ (2A)} - \overbrace{\frac{F_{\mathrm{LTGF}} * (F_{\mathrm{PLS}} + F_{\mathrm{PLS,LTGF}}) * k_{u2}}{k_{m2} + F_{\mathrm{LTGF}}}}^{Release\ TGF\ (3A)}$$

2.4.5 Plasminogen conversion into plasmin

Fibrin-bound plasminogen (F_{PLG}) can be converted to fibrin-bound plasmin (F_{PLS}). This conversion (reaction 4A) occurs in proximity of uPAR, modeled by Michaelis Menten kinetics with rate constants k_{u1} and k_{m1}. To express the proximity of uPAR, the concentration of uPAR at a certain pixel is calculated by taking the average concentration of uPAR of that pixel and of its second neighboring pixels (together forming the set of pixels $NB(\sigma)$), resulting in $U =< uPAR_{\sigma} >_{\text{NB}(\sigma)}$. The change in concentration of fibrin-bound plasminogen depends on $PLG - Fibrin$ binding (1A), $LTGF - F_{\text{PLG}}$ binding (2B), plasmin activation (4A), release of TGF (3B) and its decay, following:

$$\frac{\partial F_{\text{PLG}}}{\partial t} = \overbrace{PLG * F * k_{f1} - F_{PLG} * k_{r1}}^{PLG-Fibrin\ binding\ (1A)} - \overbrace{\frac{F_{PLG} * U * k_{u1}}{k_{m1} + F_{PLG}}}^{Plasmin\ activation\ (4A)} + \overbrace{F_{\text{PLG,LTGF}} * k_{r2} - LTGF * F_{PLG} * k_{f2}}^{LTGF-F_{\text{PLG}}\ binding\ (2B)} - \overbrace{\epsilon_{F_{\text{PLG}}} F_{\text{PLG}}}^{Decay} + \overbrace{\frac{F_{\text{PLG,LTGF}} * (F_{\text{PLS}} + F_{\text{PLS,LTGF}}) * k_{u2}}{k_{m2} + F_{\text{PLG,LTGF}}}}^{Release\ TGF\ (3B)} \tag{2.8}$$

The change in concentration of $F_{\text{PLG,LTGF}}$ depends on $PLG - F_{\text{LTGF}}$ binding (1B), $LTGF - F_{\text{PLG}}$ binding (2B), plasmin activation (4B), release of TGF (3B) and its decay, following:

$$\frac{\partial F_{\text{PLG,LTGF}}}{\partial t} = -\overbrace{\epsilon_{F_{\text{PLG,LTGF}}} F_{\text{PLG,LTGF}}}^{Decay} + \overbrace{PLG * F_{\text{LTGF}} * k_{f1} - F_{\text{PLG,LTGF}} * k_{r1}}^{PLG-F_{\text{LTGF}}\ binding\ (1B)} + \overbrace{LTGF * F_{\text{PLG}} * k_{f2} - F_{\text{PLG,LTGF}} * k_{r2}}^{LTGF-F_{\text{PLG}}\ binding\ (2B)} - \overbrace{\frac{F_{\text{PLG,LTGF}} * U * k_{u1}}{k_{m1} + F_{\text{PLG,LTGF}}}}^{Plasmin\ activation\ (4B)} - \overbrace{\frac{F_{\text{PLG,LTGF}} * (F_{\text{PLS}} + F_{\text{PLS,LTGF}}) * k_{u2}}{k_{m2} + F_{\text{PLG,LTGF}}}}^{Release\ TGF\ (3B)} \tag{2.9}$$

2.4.6 Plasmin activity

Fibrin-bound plasminogen is converted to fibrin-bound plasmin by uPAR. F_{PLS} is the conversion product of F_{PLG} (reaction 4A), and $F_{\text{PLS,LTGF}}$ is the conversion product of $F_{\text{PLG,LTGF}}$ (reaction 4B). To model fibrinolysis, F_{PLS} (reaction 5A) and $F_{\text{PLS,LTGF}}$ (reaction 5B) are degraded, modeled with a Hill equation with constant d. The change in concentration of F_{PLS} depends on plasmin activation (4A), fibrinolysis (5A), $LTGF - F_{\text{PLS}}$ binding (2C), release of TGF (3C),

and its decay, following:

$$\frac{\partial F_{\mathrm{PLS}}}{\partial t} = \overbrace{-\epsilon_{F_{\mathrm{PLS}}} F_{\mathrm{PLS}}}^{\textit{Decay}} + \overbrace{\frac{F_{\mathrm{PLG}} * U * k_{u1}}{k_{m1} + F_{\mathrm{PLG}}}}^{\textit{Plasmin activation (4A)}} - \overbrace{\frac{F_{\mathrm{PLS}}^2}{d + F_{\mathrm{PLS}}^2}}^{\textit{Fibrinolysis (5A)}} + \overbrace{F_{\mathrm{PLS,LTGF}} * k_{r2} - LTGF * F_{\mathrm{PLS}} * k_{f2}}^{\textit{LTGF}-F_{\mathrm{PLS}}\ \textit{binding (2C)}} + \overbrace{\frac{F_{\mathrm{PLS,LTGF}} * (F_{\mathrm{PLS}} + F_{\mathrm{PLS,LTGF}}) * k_{u2}}{k_{m2} + F_{\mathrm{PLS,LTGF}}}}^{\textit{Release TGF (3C)}} \tag{2.10}$$

The change in concentration of $F_{\mathrm{PLS,LTGF}}$ depends on plasmin activation (4B), fibrinolysis (5B), $LTGF - F_{\mathrm{PLS}}$ binding (2C), release of TGF (3C), and its decay, following:

$$\frac{\partial F_{\mathrm{PLS,LTGF}}}{\partial t} = \overbrace{\frac{F_{\mathrm{PLG,LTGF}} * U * k_{u1}}{k_{m1} + F_{\mathrm{PLG,LTGF}}}}^{\textit{Plasmin activation (4B)}} + \overbrace{LTGF * F_{\mathrm{PLS}} * k_{f2} - F_{\mathrm{PLS,LTGF}} * k_{r2}}^{\textit{LTGF}-F_{\mathrm{PLS}}\ \textit{binding (2C)}} - \overbrace{\frac{F_{\mathrm{PLS,LTGF}}^2}{d + F_{\mathrm{PLS,LTGF}}^2}}^{\textit{Fibrinolysis (5B)}} - \overbrace{\frac{F_{\mathrm{PLS,LTGF}} * (F_{\mathrm{PLS}} + F_{\mathrm{PLS,LTGF}}) * k_{u2}}{k_{m2} + F_{\mathrm{PLS,LTGF}}}}^{\textit{Release TGF (3C)}} - \overbrace{\epsilon_{F_{\mathrm{PLS,LTGF}}} F_{\mathrm{PLS,LTGF}}}^{\textit{Decay}} \tag{2.11}$$

2.4.7 TGFβ1 activation

Plasmin can release and activate latent-TGFβ1, resulting in active TGFβ1 (TGF) that diffuses with diffusion coefficient D_{TGF} and decays with rate ϵ_{TGF}. TGF can originate from each form of fibrin-bound latent-TGFβ1 (F_{LTGF}, $F_{\mathrm{PLG,LTGF}}$ and $F_{\mathrm{PLS,LTGF}}$), released by plasmin following Michaelis Menten kinetics with constants k_{u2} and k_{m2}. The change in concentration of TGF depends on release of TGF (3A, 3B, and 3C), and its diffusion and decay, following:

$$\frac{\partial TGF}{\partial t} = \overbrace{D_{\text{TGF}}\nabla^2 TGF}^{\textit{Diffusion}} - \overbrace{\epsilon_{\text{TGF}} TGF}^{\textit{Decay}} + \overbrace{\frac{F_{\text{LTGF}} * (F_{\text{PLS}} + F_{\text{PLS,LTGF}}) * k_{u2}}{k_{m2} + F_{\text{LTGF}}}}^{\textit{Release TGF (3A)}} + \overbrace{\frac{F_{\text{PLG,LTGF}} * (F_{\text{PLS}} + F_{\text{PLS,LTGF}}) * k_{u2}}{k_{m2} + F_{\text{PLG,LTGF}}}}^{\textit{Release TGF (3B)}} + \overbrace{\frac{F_{\text{PLS,LTGF}} * (F_{\text{PLS}} + F_{\text{PLS,LTGF}}) * k_{u2}}{k_{m2} + F_{\text{PLS,LTGF}}}}^{\textit{Release TGF (3C)}} \tag{2.12}$$

2.4.8 uPAR and PAI-1

Each cell has an individual concentration of uPAR with a constant production rate (c), a decay rate (ϵ_{uPAR}), a TGFβ1-dependent production and a PAI-1 dependent internalization. For the TGFβ1-dependent production, the total amount of TGF on all membrane pixels of a cell (P_σ) is summed and this total amount of TGF upregulates the uPAR production with Michaelis Menten kinetics, using constants k_{u3} and k_{m3}. Cells secrete PAI-1 (PAI) with rate α. PAI-1 binds uPAR for inactivation, resulting in a depletion of PAI and $uPAR$ with rate k_{f3}. For this purpose the concentration of PAI is calculated over all cell pixels (C_σ). PAI diffuses with diffusion coefficient D_{PAI} and decays with rate ϵ_{PAI}. The change in concentration of PAI depends on its internalization when bound to uPAR, its secretion, and its diffusion and decay, following:

$$\frac{\partial PAI}{\partial t} = \overbrace{-\sum_{\sigma=1}^{n}(uPAR_\sigma * PAI * k_{f3})}^{\textit{Internalization}} - \overbrace{\epsilon_{\text{PAI}} PAI}^{\textit{Decay}} + \overbrace{\alpha 1_{\tau(x)=\text{cell}}}^{\textit{Secretion}} + \overbrace{D_{\text{PAI}}\nabla^2 PAI}^{\textit{Diffusion}} \tag{2.13}$$

The concentration of $uPAR$ is homogeneously spread over the cell membrane and is continuously updated to the location of the cell. It decays with rate ϵ_{uPAR}. The change in concentration of $uPAR$ depends on its internalization when bound to PAI, a constant production, a TGF-induced production and its

decay, following:

$$\frac{\partial uPAR_\sigma}{\partial t} = \overbrace{-\sum_{i \in C_\sigma} (uPAR_\sigma * PAI(i) * k_{f3})}^{Internalization} - \overbrace{\epsilon_{\text{uPAR}} uPAR_\sigma}^{Decay} + \tag{2.14}$$

$$\overbrace{c}^{Constant\ production} + \overbrace{\frac{k_{u3}(\sum_{j \in P_\sigma} TGF(j))^2}{k_{m3} + (\sum_{j \in P_\sigma} TGF(j))^2}}^{TGF-induced\ uPAR\ production} \forall \sigma \in 1, .., 50$$

2.4.9 Numerical solution

The uPAR concentration per cell is solved numerically once every MCS, with $\Delta x = 2 \cdot 10^{-6}$ m and $\Delta t = 150$ s, and all other concentration fields are solved ten times per MCS, using an explicit finite-difference scheme. The quantitative values of the parameters involved in the plasminogen-plasmin system and uPAR-plasmin-TGFβ1 positive feedback loop are experimentally not known. We manually looked for a set of parameter values for which only a few cells in the monolayer initialized sprouting. We subsequently studied the sensitivity of the model to changes in the parameter values in Sections 2.2.2 and 2.2.3. The parameter settings for the kinetic reactions are listed in Table 2.2.

We initialize the model with a readily fibrin-bound concentration of latent-TGFβ1 and plasminogen, by setting the initial concentration $I_{F_{\text{PLG,LTGF}}}$=1 at every lattice site of type fibrin. All other concentrations are relative to this concentration level, expressed in relative units (RU). For the model validation experiments, we either reduced the level of plasminogen or of latent-TGFβ1 in the fibrin matrix and kept the other constant, by reducing the initial concentration of $I_{F_{\text{PLG,LTGF}}}$ and increasing the concentration of $I_{F_{\text{LTGF}}}$ or $I_{F_{\text{PLG}}}$ respectively.

Table 2.2: Parameter settings kinetics. The concentration of all proteins is expressed in relative units (RU) and one MCS represents approximately 2.5 minutes.

$I_{F_{PLG,LTGF}} = 1\ RU$	$\epsilon_{F_{PLG}} = 1 \cdot 10^{-4}\ MCS^{-1}$
$I_{uPAR} = 1\ RU$	$\epsilon_{F_{PLS}} = 1 \cdot 10^{-4}\ MCS^{-1}$
$\alpha = 0.01\ RU/MCS^{-1}$	$\epsilon_{F_{LTGF}} = 1 \cdot 10^{-4}\ MCS^{-1}$
$D_{PLG} = 5 \cdot 10^{-12}\ m^2/MCS$	$\epsilon_{F_{PLG,LTGF}} = 1 \cdot 10^{-4}\ MCS^{-1}$
$D_{LTGF} = 5 \cdot 10^{-12}\ m^2/MCS$	$\epsilon_{F_{PLS,LTGF}} = 1 \cdot 10^{-4}\ MCS^{-1}$
$D_{TGF} = 5 \cdot 10^{-12}\ m^2/MCS$	$\epsilon_{PAI} = 1 \cdot 10^{-2}\ MCS^{-1}$
$k_m1 = 1\ RU$	$\epsilon_{uPAR} = 9.5 \cdot 10^{-3}\ MCS^{-1}$
$k_m2 = 1.1\ RU$	$\epsilon_{PLG} = 1 \cdot 10^{-3}\ MCS^{-1}$
$k_m3 = 8\ RU$	$\epsilon_{LTGF} = 1 \cdot 10^{-3}\ MCS^{-1}$
$c = 5 \cdot 10^{-3}\ s^{-1}\ RU/MCS^{-1}$	$\epsilon_{TGF} = 5 \cdot 10^{-2}\ MCS^{-1}$
$k_f1 = 1 \cdot 10^{-2}\ MCS^{-1}RU^{-1}$	$k_u1 = 1\ MCS^{-1}$
$k_f2 = 1 \cdot 10^{-2}\ MCS^{-1}RU^{-1}$	$k_u2 = 0.8\ MCS^{-1}$
$k_f3 = 1 \cdot 10^{-2}\ MCS^{-1}RU^{-1}$	$k_u3 = 0.85\ MCS^{-1}$
$k_r1 = 1 \cdot 10^{-4}\ MCS^{-1}$	$d = 4 \cdot 10^{-2}\ RU^2$
$k_r2 = 1 \cdot 10^{-8}\ MCS{-}1$	

2.A Supplementary movies

An archive containing all supplementary movies can be found at
`http://persistent-identifier.org/?identifier=urn:nbn:nl:ui:18-23531`.

Movie S1 **Sprouting by the uPAR-plasmin-TGFβ1 positive feedback.** This movie shows the selection of ingrowth spots in the endothelial cell monolayer and further sprouting due to the uPAR-plasmin-TGFβ1 positive feedback in a simulation with default parameter settings. The movie is divided in four panels. The top left panel shows the CPM representation of cells (blue) and fibrin (yellow). The top right panel shows the concentration of uPAR in the cells. The bottom left frame shows the concentration of active TGFβ1 and the bottom right panel shows the concentration of PAI-1. Protein concentrations are colored according a color bar, with red indicating the highest concentration in the current field and blue the lowest concentration.